Understanding the Photothermal and Photocatalytic Mechanism of Polydopamine Coated Gold Nanorods

Daniel Aguilar-Ferrer, Thomas Vasileiadis, Igor Iatsunskyi, Marcin Ziółek, Klaudia Żebrowska, Olena Ivashchenko, Paulina Blaszkiewicz, Bartosz Grześkowiak, Raquel Pazos, Sergio Moya, et al.

ADVANCED FUNCTIONAL MATERIALS
www.afm-journal.de

Understanding the Photothermal and Photocatalytic Mechanism of Polydopamine Coated Gold Nanorods

*Daniel Aguilar-Ferrer, Thomas Vasileiadis, Igor Iatsunskyi, Marcin Ziółek, Klaudia Żebrowska, Olena Ivashchenko, Paulina Błaszkiewicz, Bartosz Grześkowiak, Raquel Pazos, Sergio Moya, Mikhael Bechelany, and Emerson Coy**

Localized surface plasmon resonance (LSPRs) shown by gold nanorods (AuNRs) has several applications in photocatalysis, sensing, and biomedicine. The combination of AuNRs with Polydopamine (PDA) shells results in a strong photo-thermal effect, making them appealing nanomaterials for biomedical applications. However, the precise roles and relative contributions of plasmonic effects in gold, and light-to-heat conversion in PDA are still debated. Herein, a hybrid nanoplatform made by an AuNR core surrounded by a polydopamine (PDA) shell is synthesized, and its photocatalytic behavior is studied. Synthesis is based on a seed-mediated growth followed by the further self-polymerization of dopamine hydrochloride (DA) on the surface of the AuNRs, and the effect of the thickness of the PDA shell on the plasmon response of the composite is the main examined parameter. Photocatalytic performance is tested toward Rhodamine 6G (Rh6G), with the nanocomposites achieving better performance than bare AuNRs and bare PDA nanoparticles. The degradation of 54% of Rh6G initial concentration is achieved within 60 min of irradiation with a catalyst concentration of 7.4 μg mL^{-1}. Photodegradation kinetics, time-resolved spectroscopy, and finite-element-method simulations of plasmons show that AuNRs plasmons, coupled with the low thermal conductivity of PDA, provide slow thermalization, while enhancing the charge carrier transfer.

1. Introduction

Due to confinement effects, metallic nanostructures can display optical, electrical, and catalytic properties different from their bulk counterparts. Illumination of nanometals with light can trigger collective oscillations of free electrons in the metallic nanostructure, which are termed localized surface plasmons (LSP). When the external frequency reaches the plasma frequency of the metal (resonance), it absorbs the incident light, creating strongly localized and amplified electric fields in the vicinity of the particle surface. This phenomenon, called LSP resonance (LSPR), depends on the particle shape, size, density of electrons, dielectric properties of the metal, and its surrounding medium.[1–3] The energy presented by LSP can decay in two different manners: by the non-radiatively generation of hot electrons or radiatively, meaning by re-emission of light.[4,5] These processes can be used in photochemistry due to the inherent conversion of light to free electrons or thermal energy. Gold nanoparticles (AuNPs) and gold nanorods (AuNRs) have been recently applied in several fields, such as optics, electrochemistry, biological sensing,[6] and catalysis.[7–11]

AuNPs and AuNRs have recently been combined with the biomimetic polymer polydopamine (PDA), with promising results for photocatalysis. Au/PDA composites on glass substrates (Au/PDA@slide) have been proven to photodegrade methyl orange and reduce 4-nitrophenol at room

D. Aguilar-Ferrer, I. Iatsunskyi, K. Żebrowska, O. Ivashchenko, B. Grześkowiak, E. Coy
NanoBioMedical Centre
Adam Mickiewicz University
Wszechnicy Piastowskiej 3, Poznan 61-614, Poland
E-mail: coyeme@amu.edu.pl

The ORCID identification number(s) for the author(s) of this article can be found under https://doi.org/10.1002/adfm.202304208

DOI: 10.1002/adfm.202304208

D. Aguilar-Ferrer, M. Bechelany
Institut Européen des Membranes
IEM
UMR 5635
University of Montpellier
ENSCM
Centre National De la Recherche Scientifique (CNRS)
Montpellier 34730, France

T. Vasileiadis, M. Ziółek
Faculty of Physics
Adam Mickiewicz University
Uniwersytetu Poznańskiego 2, Poznań 61-614, Poland

P. Błaszkiewicz
Faculty of Materials Engineering and Technical Physics
Poznan University of Technology
Piotrowo 3, Poznan 60-965, Poland

temperature with $NaBH_4$ as a reducing agent.[12] Reduction of 4-nitrophenol can also be carried out by Au@PDA nanoreactors driven by infrared irradiation with an assembled block copolymer of polystyrene-b-poly(2-vinylpyridine) [Ps-*b*-P_2VP] nanosphere used as a soft template. A reduction of 1.1% without near-infrared (NIR) irradiation at room temperature is observed, while with an increase of temperature to 39.3 °C the reduction reaches 48.4%. Under NIR irradiation at a high enough fluence, the reduction goes to 89.9%.[13] Apart from environmental applications, PDA and AuNPs have shown promising results in nanomedicine. For instance, layer-by-layer Au-PDA(core)@PDA(shell) sandwiches have been proven to have photo-thermal performance at 808 nm, mainly due to the synergistic effect of the Au plasmonic effect and the thermal properties of PDA. Because of all this, Au/PDA shows a promising application in photo-thermal cancer therapy.[14] Furthermore, due to the easy functionalization with PDA,[15] AuNRs/PDA can be used as drug carriers and loaded with several drugs for tumor treatment, such as methylene blue (MB) or doxorubicin (DOX), which can be adsorbed on the surface, creating different nanocomposites. AuNRs/PDA-MB, can generate reactive oxygen species (ROS) or hyperthermia, and the second one, AuNRs/PDA-DOX, can release DOX when NIR light is applied.[16] Besides, AuNRs/PDA nanocomposites presenting plasmonic extinction at NIR can be loaded with Rhodamine 123 for strong fluorescence under UV–vis excitation and be functionalized with folic acid for enhanced cellular uptake.[17] Nanocomposites can selectively accumulate in folate-positive HeLa cells but not in folate-negative HEK 293, thereby combining targeting cancer cells and NIR light-mediated phototherapy.[17,18] Finally, in another application, PDA has been used for caging AuNRs onto the surface of PEGylated graphene oxide to create hybrid nanosheets, which can be used efficiently as drug carriers and in photo-thermal therapy (PTT).[19]

Furthermore, by creating heterojunctions, PDA has been shown to increase the photocatalytic behavior of different semiconductors, such as TiO_2, ZnO, or Fe_3O_4.[20] However, the role of the PDA coatings in metallic systems is not clear since PDA alone does not show strong degradation of contaminants,[21,22] and no heterojunction or bandgap bending takes place, as in the case of other photoactive composites.[20]

Therefore, although the applications for Au/PDA nanocomposites are rather well established, the electronic effects of PDA coating on the Au particles remain unexplored, and the mechanism behind their photo-thermal and photocatalytic applicability is still debated. This is especially challenging since these nanocomposites exhibit properties that bare Au and PDA nanoparticles do not possess. In this study, we aim to understand the origin of this effect by combining photocatalytic/photo thermals experiments, modelling, and time-resolve spectroscopy methods. Here we will show that Au/PDA composites produce significantly larger amounts of reactive oxygen species (ROS) at different wavelengths. Moreover, we will show that thermal effects do not enhance ROS production but can be controlled by increasing the thickness of the PDA coating, which, surprisingly, does not hinder ROS production but augments it. Our study brings a fundamental understanding of the role of thermal effects in plasmonic nanocomposites and a general explanation of the Au/PDA photo-thermal/photocatalytic effects for environmental and biomedical applications.

2. Experimental Section

2.1. Synthesis of Au Nanorods

Aqua regia (HCl:HNO_3 3:1 v/v) was used to treat glass prior to the synthesis process of nanorods (AuNRs). In the overall synthesis process, ultrapure water (Milli-Q, 18.2 MΩ cm, 71.98 ± 0.01 mN m^{-1}) was used. AuNRs were synthesized by a seed-mediated growth method.[23] Seed solution was made, at 37 °C, by the addition of $HAuCl_4$ (Sigma–Aldrich, ≥99.9, 0.01 M, and 0.25 mL) into cetyltrimethylammonium bromide (CTABr) (Sigma–Aldrich, ≥98%, 0.1 M, and 9.75 mL). After it was mixed, an ice-cold $NaBH_4$ solution (Acros Organics, 99%, 0.01 M, and 0.60 mL) was gently added with vigorous stirring for a few seconds. The seed solution is kept at room temperature for 2 h for further use. The growth solution was prepared by mixing, in this order, CTABr (0.1 M, 40 mL) $HAuCl_4$ (0.01 M, 2.0 mL) $AgNO_3$, (Sigma–Aldrich, ≥99.0%, 0.01 M, and 0.40 mL), HCl (Stanlab, 35–38%, 1.0 M, and 0.80 mL), and ice-cold ascorbic acid (Sigma–Aldrich, ≥99%, 0.1 M, and 0.32 mL) after the mixture was completed, 0.040 mL of seed solution were added. The growth process took place when the seed solution was added at a temperature of 27–30 °C. The final solution was stirred for a few seconds and then was kept covered by an aluminum foil for 24 h at room temperature. After the synthesis process, the reaction product was fractionated correctly and purified by centrifugation and removal of the supernatant. AuNRs were obtained with a transversal face of 18.0 ± 2.4 nm, and a longitudinal length of 81.6 ± 9.3 nm.

2.2. Synthesis of AuNRs/PDA Nanocomposites

AuNRs/PEG were prepared by the previous substitution of AuNRs capping agent (CTABr) by (poly(ethylene glycol) methyl ether thiol, MW = 6000),(SH-PEG-CH_3). 40 mL of AuNRs were centrifuged twice at 12 000 rpm for 12 min. The pellet was dispersed in 25 mL of an aqueous solution of PEG (Sigma–Aldrich, 2 mg mL^{-1}, MW = 6000), vortexed, and stirred for 20 h. This procedure repeated, and AuNRs/PEG were collected by centrifugation.

AuNRs/PDA were prepared by dispersion of AuNRs/PEG in tris buffer (pH ≈8.5).[16] This dispersion was vortexed and sonicated for 5 min. After this procedure, a dopamine hydrochloride aqueous solution was added to have a final concentration

R. Pazos
Chromatography & Mass Spectrometry Platform
CIC biomaGUNE
Paseo Miramón 182, San Sebastián 20014, Spain
S. Moya
Soft Matter Nanotechnology
Centre for Cooperative Research in Biomaterials (CIC biomaGUNE)
Basque Research and Technology Alliance (BRTA)
Paseo Miramon 182 C, Donostia-San Sebastian 20014, Spain
M. Bechelany
Gulf University for Science and Technology (GUST)
Hawalli 32093, Kuwait

of dopamine hydrochloride (Sigma–Aldich) of 0.5 mg mL^{-1}. The mixed solution was vortexed and sonicated for 30 min, and then the final product was collected by centrifugation: 2 times at 10 000 rpm for 10 min. AuNRs/PDA hybrids showed 30.45 ± 4.9 nm shell thickness, transversal LSPR of 514 nm, and a longitudinal LSPR of 806 nm. To obtain other PDA shell lengths, hence other LSPR values, the final dopamine hydrochloride concentration was modified to: 0.085, 0.125, and 0.25 mg mL^{-1} obtaining AuNRs/PDA1, AuNRs/PDA2 and AuNRs/PDA3. (Table S1, Supporting Information)

2.3. Characterization Methods

Transmission Electron Microscope (TEM) images were taken with a JEOL 1400 microscope operating at 120 kV. UV/Vis spectra were obtained on a Lambda 950 (Perkin Elmer), and FT/IR 4700LE (Jasco) was used to collect the Fourier Transform Infrared (FTIR) spectra. For ICP-MS quantification, samples were digested using HNO_3 and HCl and then measured with a Perkin Elmer Analyst 800 ICP-MS. Thermal imaging experiments were collected with a thermal camera Sonel KT-650. Finally, transient absorption (TA) spectroscopy was performed using a Helios Spectrometer (Ultrafast System) and Spectra-Physics fs laser system. The instrument response function was ≈200 fs (full width at half-maximum), and transient absorption measurements were performed in the time range of up to 3 ns. Samples were suspended in water and examined in a quartz cuvette of 2 mm thickness. To obtain characteristic time constants of the observed ultrafast processes, global analysis in the broad spectral probing range of 430–830 nm was performed, in which selected singular value (SV) kinetic vectors were analyzed using Surface Explorer (Ultrafast Systems) software. The dominant 1st SV kinetic vector was chosen, as the other kinetic vectors represented the contribution of solvent artifacts[24] and the random noise. Due to the spectrometer limitations, shorter AuNRs were synthesized (≈75 ± 2 nm in length and ≈20 ± 3 nm in width), so the longitudinal plasmon would remain within the spectrometer range.

2.4. Photocatalysis

Photocatalytic experiments were carried out in a quartz cuvette placed 10 cm away from the light source. The target organic dye was Rhodamine 6G (Rh6G) with a final concentration of $[Rh6g]_f$ = 2.5 μg mL^{-1} using bare AuNRs, PDA spheres (average size of 90 ± 10 nm) AuNRs/PDA1, AuNRs/PDA2, and AuNRs/PDA3 as potential catalysts. The final catalyst concentrations were the same for all the experiments (7.4 μg mL^{-1}). A Xenon Sciencetech lamp model illuminated the samples: LH-E-300X, with variable power (0.02–2.5 W) over a 0.55 cm radius spot for 1 h. The UV–vis spectra of each catalyst were used as a reference/background to have a clear Rh6G signal (Figure S1, Supporting Information). The absorbance spectrum of Rh6G was measured every 5 min using a Lambda 950 (Perkin Elmer) instrument. Also, the temperature was recorded every 3 min with a thermal camera (Sonel KT-650) and every minute with a thermocouple.

ROS determination and scavengers test were performed using Ethylenediaminetetraacetic acid (EDTA) (Sigma–Aldrich, 99.4–100.6%), isopropyl alcohol (IPA) (Avantor Performance Materials Poland) and p-benzoquinone (BQ) (Sigma–Aldrich - Synthesis graded).

2.5. Modeling and Calculations

Calculations of the electromagnetic (EM) fields, EM losses, and heating were performed based on the finite-element-method (FEM), and the commercially available software COMSOL Multiphysics. Au nanorods were designed as two semi-spherical caps connected by a cylinder. The length of the nanorods (L), which corresponded to the experimental definition, was defined as the maximum distance between apexes, according to Figure S2a (Supporting Information). The nanostructure was then placed at the center of a spherical volume filled with water and surrounded by spherical perfectly matched layers (PML in Figure S2b, Supporting Information). The equations were solved for the scattered field, using a background electric field of the form: $\vec{E}_0 \exp(-j\, k\, \gamma)$, where $\vec{E}_0$ could be parallel to the long NR axis (termed longitudinal polarization) or normal to the long NR axis (transverse polarization). The $\vec{E}_0 = \sqrt{2\, I_0/(c\, \varepsilon_o\, \sqrt{\varepsilon_r})}$, where I_0 is the intensity of light. The beam had a flat-top profile in agreement with the experiments. Table S2 (Supporting Information) gives the comparison of experimental and theoretical light wavelengths for transverse and longitudinal plasmonic resonances.

For the calculations with the lamp, the power of each wavelength was set such that we reproduce the lamp spectrum and its total power. The reduced absorption of Au (Figure S3a, Supporting Information), and the enhanced absorption of PDA (Figure S3b, Supporting Information), as observed for the VIS experiments, is due to the increased imaginary part of the refractive index of PDA close to the VIS spectrum maximum (Figure S3c, Supporting Information).

Photocatalytic experiments in this study did not use sufficiently high light intensities to create considerable ultrafast heating near the nanostructures. To achieve discernible localized heating, visible light with tens of mW power must be focused on a spot with a diameter ≤10 μm. This was demonstrated in the final-state calculations of Figure S4 (Supporting Information).

For the simulations of macroscopic heat transfer (Figure S5, Supporting Information) a quartz cuvette (Hellma, no. 101-10-40) on a thermoplastic surface (polyethylene) was designed, filled with 3 mL of water and ≈$40{\cdot}10^9$ NRs mL^{-1} (7 μg mL^{-1}). In this way, the light focus (lamp or laser) was treated as a cylindrical, macroscopic heat source within the water. Due to their low concentration, the contribution of the nanostructures to the thermal properties of water is negligible. The faster thermalization times observed in the experiments are due to the steering of the solutions.

3. Results

3.1. Synthesis of AuNRs/PDA

As shown in **Figure 1**a, the synthesis of AuNRs/PDA was divided into two main steps. The first step consists of seed-mediated growth[23] followed by the second step, which is a substitution

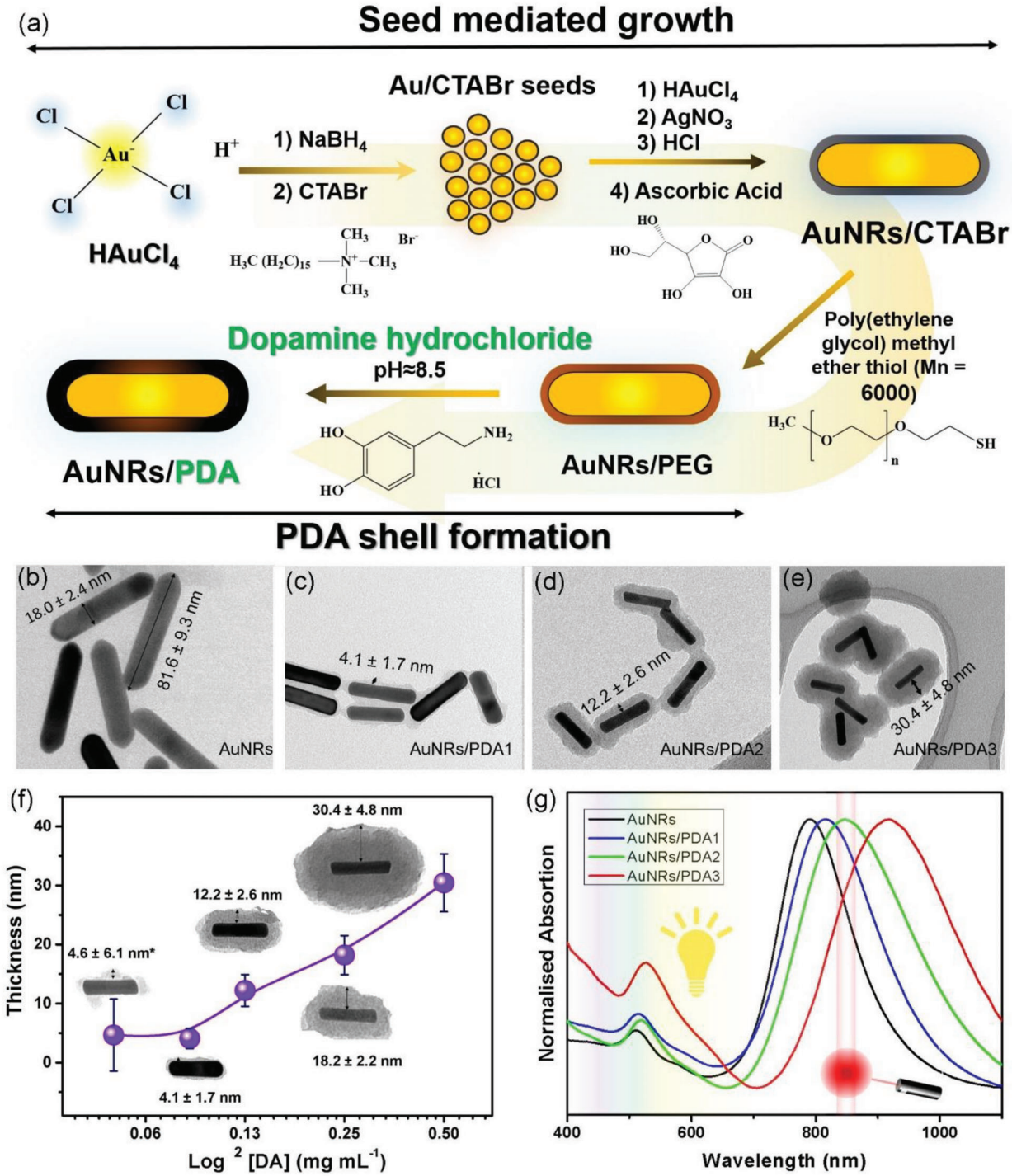

Figure 1. a) Scheme of AuNRs/PDA synthesis divided into two main steps; seed-mediated growth of AuNRs and further PDA self-polymerization on the AuNRs surface. TEM images: b) Bare AuNRs, c) AuNRs/PDA1, d) AuNRs/PDA2, and e) AuNRs/PDA3. f) PDA shell thickness (with SD) versus $\log^2$[DA] with the corresponding AuNRs/PDA nanocomposites TEM images at the insets. The solid line is a guide to the eye. g) Transversal and longitudinal LSPR values showed by AuNRs, AuNRs/PDA1 AuNRs/PDA2, and AuNRs/PDA3. Color insets show the regions of VIS and NIR (808 nm).

of CTABr by PEG for further self-polymerization of dopamine on its surface.[16] Seed-mediated growth was based on creating tiny nucleation gold centers where AuNRs can grow. Nucleation centers are formed from the gold precursor ($HAuCl_4$) seed solution. The procedure involves reducing Au^{3+} to Au^0 by using $NaBH_4$ as a reducing agent. The reaction temperature (up 27 °C) and a suitable CTABr concentration are crucial for fabrication of stable and homogenous AuNRs of a desired aspect ratio. A CTABr bilayer on the surface of AuNRs shields against conglomeration, and the addition of $AgNO_3$ to the growing solution

promotes the regulation of the aspect ratio and anisotropic development. By mixing growth and seed solution, Ag from $AgNO_3$ was reduced to Ag^0 only at the longitudinal surface of the AuNR, avoiding the deposition of gold there and forcing rod-shaped growth. Once AuNRs are synthesized, the adsorption of positively charged CTABr molecules on their surface avoids the adsorption of dopamine. To overcome it, CTABr was replaced with thiolated polyethylene glycol, which interacts more strongly with the Au surface and can resist the alkaline pH value necessary for the dopamine to self-polymerize, preventing particle aggregation.

As expected, the thickness/density of the PDA shell can be controlled by dopamine concentration. In Figure 1b–e, we show bare Au NRs and three Au/PDA composites with different average shell thicknesses 4.1 ± 1.7 nm called AuNRs/PDA1(Figure 1c), 12.2 ± 2.6 nm called AuNRs/PDA2 (Figure 1d) and 30.4 ± 4.8 nm called AuNRs/PDA3 (Figure 1e). Their PDA shell length distribution histogram (Figure S6, Supporting Information) shows that the samples were homogeneous, and the measured values fitted in a Gaussian bell function. Figure 1f, shows the relation between dopamine hydrochloride concentration and the thickness of the shell. It is important to mention that DA concentration of $[DA]_f = 0.05$ mg mL^{-1} produced inhomogeneous coatings, while $[DA]_f = 0.25$ mg mL^{-1}, resulted in a similar thickness as AuNRs/PDA2. Therefore, these particles were not included in further studies aiming to investigate the effect of different PDA shell thicknesses.

FTIR spectra were carried out to confirm that DA had been polymerized at the surface of the AuNR forming a PDA shell. The absorption band of AuNRs/PDA presents stretching vibrations of –OH and N–H whose signal appears at ≈3200 cm^{-1}, and the peaks between ≈1500 and ≈1630 cm^{-1} are attributed to C=N, C=C, and C=O[25] (Figure S7, Supporting Information).

As LSPR depends on the surrounding medium (among other variables) of the plasmonic material, possible variations in LSPR values of gold plasmonic particles covered by the light-absorbing PDA were investigated. Results are shown in Figure 1g, where it can be noticed that both longitudinal and transversal LSPR, are redshifted when compared with the absorption spectra of the bare AuNRs (790 nm). This redshifting has been previously studied on AuNRs when covered by PDA[26] and, as is expected, changes in LSPR values are more noticeable when the PDA shell is thicker, going from 806 nm (AuNRs/PDA1) to 917 nm (AuNRs/PDA3) (see Table S1, Supporting Information).

Having prepared and characterized three distinctive nanocomposites of Au/PDA, we explored their photocatalytic performance in photodegradation applications, first upon radiation in the visible spectra.

3.2. Photodegradation Studies

3.2.1. Photodegradation Studies Under Visible Light

To compare the efficiency of nanocomposites toward the degradation of Rh6G, first, we use bare AuNRs. As shown in **Figure 2**a, AuNRs alone demonstrate a marginal performance of ≈7%, which is superior to control experiments. Interestingly, AuNRs/PDA1 show negligible increment over bare nanorods, with a 9% degradation. However, in the case of AuNRs/PDA2 and AuNRs/PDA3 (absorption spectra in Figure S8, Supporting Information), the degradation increased rapidly, from 15% and 51%, respectively. Results show that PDA NPs (≈95 nm, Figure S9, Supporting Information) and AuNRs alone cannot trigger a remarkable Rh6G degradation. Nevertheless, the hybrid composites offer better photocatalytic yield, which is clearly influenced by the thickness of the PDA shell.

Stability tests were performed by recovering the AuNRs/PDA3 catalyst by centrifugation (6.5 min, 7500 RPM) after 1 h of reaction. Recovered catalysts were redispersed in fresh Rh6G solution. Results, shown in Figure 2b, evidence that AuNRs/PDA3 are stable for two more cycles, but the photocatalytic behavior decreases ≈41% for the second cycle and ≈51% for the third cycle. This behavior can be explained by the loss of catalyst during the cleaning process and the sticky nature of PDA. Furthermore, we also studied the evaporation rate of the samples in each run. In the initial test, 2.63% of the weight is lost in the first cycle providing an evaporation rate of 888 μg min^{-1}, 2.05% in the second cycle with an evaporation rate of 686 μg min^{-1} and finally, 1.91% with an evaporation rate of 643 μg min^{-1}. The decrease in evaporation rate supports the catalyst loss during the cleaning process rather than the worsening of its catalytic performance. The relatively high evaporation rate might be associated with the known thermal properties of the Au/PDA composite. Thus, the temperature increment due to light illumination is also recorded by means of a thermocouple and a thermal camera. The temperature increment (Δ) was recorder as ≈Δ6 °C, for bare PDA NPs. Meanwhile, for AuNRs, the increment was ≈Δ7.5 °C (Figure S10, Supporting Information). The highest increment was observed for AuNRs/PDA3 with an increment of ≈Δ32.4 °C. When irradiated with light, the temperature increased sharply for ≈17 min, reaching its maximum and remaining stable for the experiment course. This behavior was also observed in all the cycles. The maximum temperature reached by AuNRs/PDA3 is shown in Figure 2c. In the first cycle, it is 56.2 °C (Δ32.4 °C), decreasing to 48.3 °C (Δ21.1 °C) in the second cycle and finally, in the last cycle, reaching 44.7 °C (Δ13.7 °C). It is clearly noticeable that for AuNRs/PDA3, temperature increases higher than for PDA NPs and AuNRs, proving that the combination of the properties of the materials leads to this behavior.

Although it is known that plasmons can drive photocatalytic processes[27,28] (**Table 1**), their performance is often presented in combination with other known semiconductor materials,[29,30] as noble metals are relatively poor catalysts in comparison to other metals, that is, d-band metals (Pt, Rh, or Pd). Quite recently, a study has shown that the combination of metals in nanoparticles might improve the photo generation of h_2 by plasmonic effects,[31,32] Herran et al, have shown that a combination of Au and Pd provides ≈3-folds enhancement of the H_2 production when compared to Au alone. Although they have not reported photodegradation of contaminants, it is expected that the high yield of production of hot holes at 2.6–2.8 eV could drive the reactions.[33] Despite this, limited studies have discussed the efficiency of AuNRs in photocatalytic applications. A recent study[34] has shown the efficiency of plasmonic effects in the photodegradation of contaminants. In this study, AuNRs were partially coated with silica shells leading to a higher thermal effect on the particles and photodegradation of contaminants. However, the catalytic enhancement was not strictly related to the

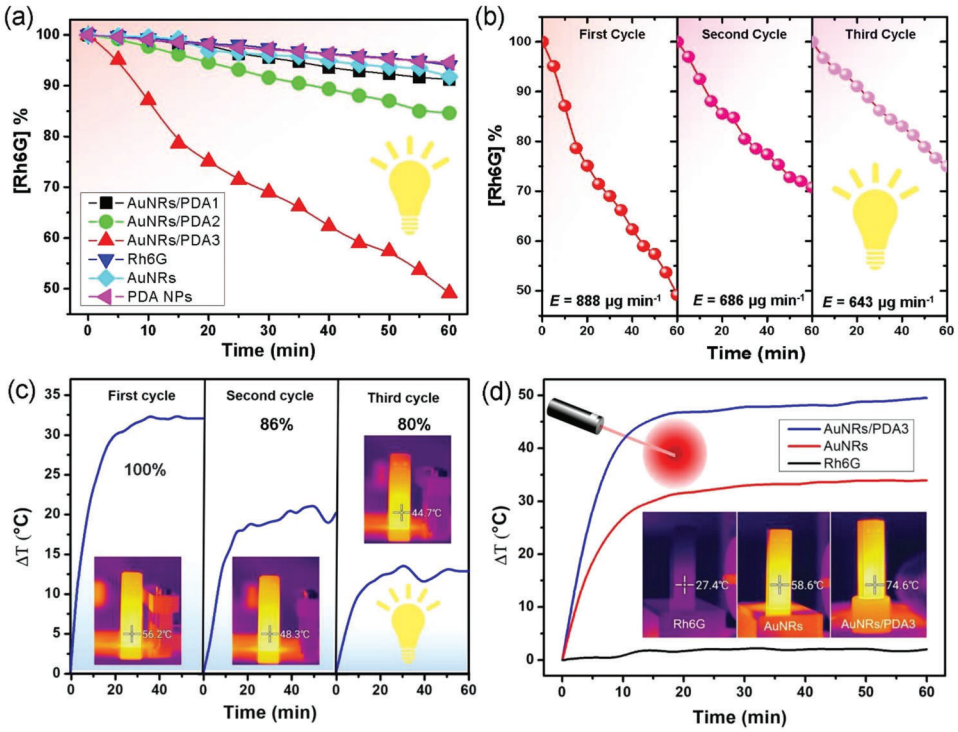

Figure 2. a) Percentage of Rh6G concentration depleted versus time, during 1 h of photocatalysis, for AuNRS/PDA1, AuNRs/PDA2, AuNRs/PDA3, Rh6G, PDA NPs, and bare AuNRs. b) Rh6G concentration percentage versus time for three consecutive photocatalysis cycles with the same sample of AuNRs/PDA3. Evaporation rate and degradation percentage at the insets c) Temperature increment, measured by thermocouple versus time for three consecutive rounds of the same sample of AuNRs/PDA3 when illuminated with the photocatalysis lamp. In-set shows thermal camera snapshots taken after 60 min. d) Temperature increment using laser and thermal camera images when maximum temperature is reached on the insets.

increment of bulk water heat, but it was a combination of electron shuttling and plasmonic effects (bulk/localized heating and hot electron transfer).

Even though our composites showed outstanding bulk water heat (photo-thermal effect) under visible light, it is crucial to determine the driving force behind the observed photocatalyst enhancement, especially since previous studies suggest that thermal effects are not the main driving force behind enhanced photodegradation. However, first, we will investigate the photodegradation and photo-thermal performance of the Au/PDA nanocomposites using NIR irradiation.

3.2.2. Photodegradation Studies Under 808 nm Laser

A main focus for the applications of AuNRs/PDA to this day has been their use in biomedicine as enhancers of photothermal therapy. **Table 2**, compiles the general literature on thermal effects induced by light on PDA-based and Au/PDA

Table 1. Catalytic response of different nanocomposites according to their concentration, organic dye concentration and time.

Nanocomposite	[Nanocomposite] [μg mL^{-1}]	Time [min]	Organic dye	Organic dye concentration [μg mL^{-1}]	Degradation [%]
AuNRs (this work)	7.4	60	Rh6G	2.5	7
PDA NPs (this work)	7.4	60	Rh6G	2.5	6
AuNRs/PDA (this work)	7.4	60	Rh6G	2.5	51
PDA[35]	100	150	Methyl orange (MO)	20	≈26
AuNPs[36]	160	55	MB	10	76
Au-ZrO_2[37]	1000	60	Sulforhodamine B (SBR)	28	64
Au-SiO_2[37]	1000	60	SBR	28	44
Au- Zeolite Y[37]	1000	60	SBR	28	51
Janus AuNRs[34]	–	120	Amoxicilin	37	43
Janus AuNRs[34]	–	120	Perfluorooctanoaic acid (PFOA)	41	10
Janus AuNRs[34]	–	25	Bisphenol A (BPA)	23	100

Table 2. Temperature increment of different nanocomposites according to their concentration, light source wavelength, and density power used..

Nanocomposite	Nanocomposite concentration [μg mL^{-1}]	Density power [mW cm^{-2}]	λ [nm]	ΔT [°C]
AuNRs (this work)	7.4	2630	UV–vis	7.5
AuNRs (this work)	7.4	2630	808	33.5
PDA NPs (this work)	7.4	2630	UV–vis	6
PDA NPs (this work)	7.4	2630	808	2.4
AuNRs/PDA (this work)	7.4	2630	UV–vis	32.4
AuNRs/PDA (this work)	7.4	2630	808	49.5
PDA[14]	100	1500	808	≈20.8
PDA NPs[40]	200	2000	808	29.6
PDA[41]	200	2000	808	30
Au@PDA[13]	500	3000	808	28.8
Au-PDA[14]	100	1500	808	≈22.6
Au-PDA@PDA[14]	100	1500	808	≈36.4
AuNRs-PDA-PEG[16]	≈18–20*)	2000	808	≈25
Mxene@Au/PDA[42]	40	2000	808	≈20
polydopamine@UiO-66[43]	50	500	980	≈20
Lipid-coated PDA[44]	100	2709	808	16
CuPDA (51 nm)[45]	100	3500	808	42.2
AuNRs@CuPDA[46]	150	3000	808	≈55
PDA@FolicAcid[47]	200	1000	808	47
PDA carbon dots[41]	200	2000	808	27
Fe_3O_4@PDA (15.5 nm) superparticles[48]	200	3500	808	66.7
Fe_3O_4-Au-PDA hybrid microcapsules[49]	200	2000	808	45
Fe_3O_4@Au/PDA core-shell hollow microspheres[49]	200	2000	808	49
Au-Ag@PDA (34 nm)[50]	800	3000	808	≈60

*) Concentration was extracted from the cited reference by assuming that the reported 0.1 nM concentration, referred to individual particles. The estimated value was extracted by calculating the amount of gold per NPs.

composites. Though the general idea of bio-applications is to use the biological window (808 nm) as a tool to induce localized heat in the nanocomposites, the increment of temperature is rather well studied, and the temperature enhancement of bare Au NPs, has been established to increase linearly with the irradiance.[38] As observed in Table 2, large power densities are typically used to generate equally important temperature variations.

Here, photodegradation and thermal tests were carried out by substituting the xenon lamp with an 808 laser to examine NIR radiation and its effects on the degradation of organic dyes. Experiments were carried out following the same procedure as with the xenon lamp (1 h of total time, $[Rh6g]_f = 2.5$ μg mL^{-1}, $[AuNRs/PDA3]_f = 7.4$ μg mL^{-1} at room temperature. First, a control test using only Rh6G was carried out, showing that the temperature increment was 2.3 °C, and then, AuNRs/PDA3 and bare AuNRs were tested. Results show a higher temperature increment than the data obtained when the xenon lamp was used. AuNRs/PDA nanocomposites showed an increment in temperature of Δ49.5 °C, reaching a maximum temperature of 74.6 °C. In comparison, the temperature increment of the bare AuNRs solution is Δ33.5 °C with a maximum temperature of 58.6 °C (Figure 2d). In both situations, the temperature increment is much higher than when the Xenon lamp is used. This increment is attributed to the near-infrared laser activation of the longitudinal plasmon presented in AuNRs/PDA3, and bare AuNRs.

Even though the temperature increment is much higher when the laser is used instead of the lamp, the degradation efficiency decreases for both, AuNRs/PDA3 nanocomposites and bare AuNRs. The degradation reaches 25% of the initial concentration of Rh6G depleted when AuNRs/PDA3 are used and 2% when bare AuNRs are employed. Moreover, additional experiments were carried out to assess the effect of temperature on the degradation process, especially since the temperature can induce ROS production.[39] Thus a Rh6G solution was heated to both maximum temperatures that can be achieved macroscopically by the Xenon lamp and the 808 nm laser. The results showed a degradation of 4% when the temperature is increased to the lamp values (56.2 °C) and 8%, when the temperature matches the laser (74.6 °C).

Therefore, it is clear that although a high temperature can be reached in NIR, and its effect on the degradation of contaminants is not negligible, it is not a leading aspect of the degradation of Rh6G. Moreover, it points to ROS generation as the phenomena behind the photodegradation observed in both cases. Nevertheless, it is crucial to explore first the photo-thermal effect observed for both the VISIBLE range and the NIR, taking into account the experimental macroscopic (bulk water heat) and the nanoparticles.

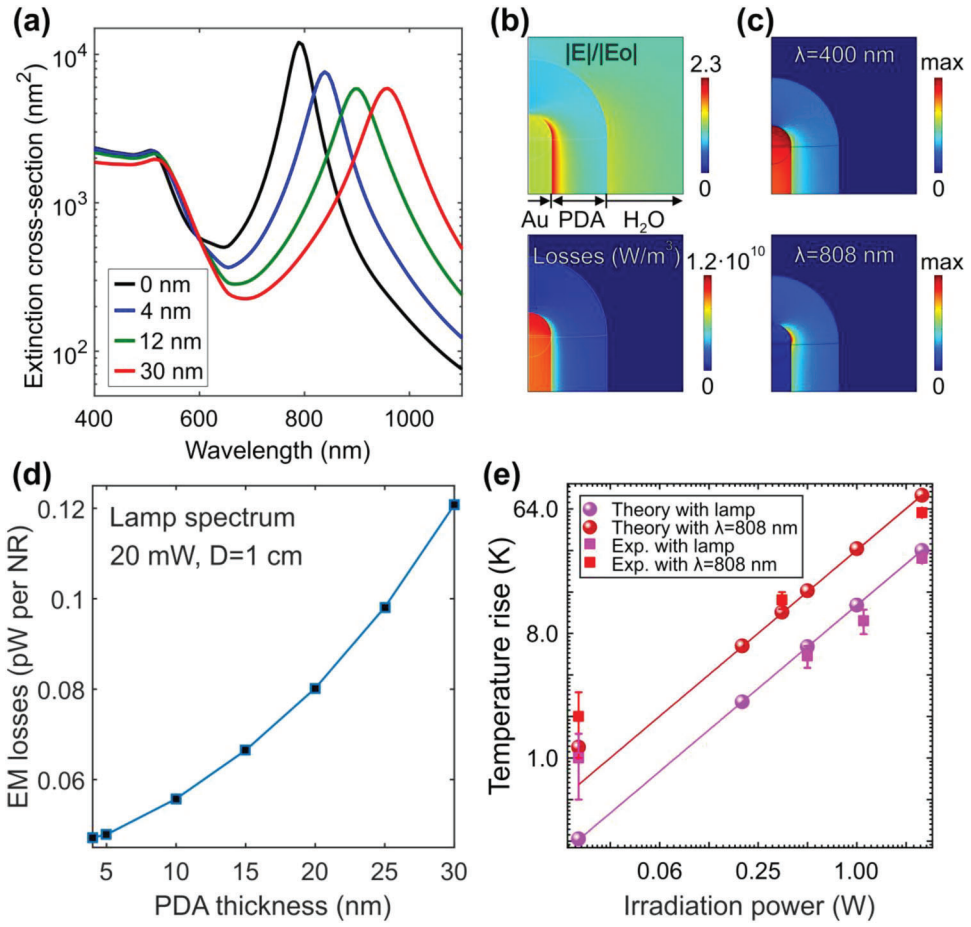

Figure 3. Finite element method simulations of plasmonic heating in aqueous dispersions of AuNR/PDA nanoparticles. a) Calculated extinction cross-section spectra of Au NRs with a thick PDA coating of 0, 4, 12, and 30 nm. b) Spatial distribution of plasmonic enhancement (up) and EM losses (down) for an Au NR with 30 nm PDA thickness, 520 nm laser wavelength, transverse polarization (incident electric field vertical to NR long axis), 20 mW power, and 1 cm focus diameter. c) Spatial distribution of EM losses for 400 (up) and 808 nm (down) light wavelengths with transverse polarization. d) Total EM losses (pico-Watt) per NR as a function of the PDA thickness with the lamp, 20 mW power and 1 cm focus diameter. e) Final temperature rise of the aqueous dispersion as a function of the irradiation power for the lamp (magenta), 808 nm wavelength (red), based on theory (circles), and experiments (squares). The solid lines are linear fittings of the calculated data with an intercept at 0 K.

3.3. Modeling of Thermal Behavior

In order to correlate macroscopic observations with nanoparticles characteristics, we first consider the measured extinction spectra. The extinction spectra is found to resemble that of a Au NR of L = 85 nm length and D = 24 nm diameter (Figure S2, Supporting Information). The length derived from the optical properties is slightly longer than the TEM results (Figure S6, Supporting Information), potentially due to the nonlinear increase of the light-scattering efficiency as a function of the nanoparticle size. For the wavelength-dependent real and imaginary refractive indices of PDA we have used values from the literature,[51–54] and we obtained the best results from that of ref.[54] The calculated extinction cross-section spectra of the Au NR /PDA systems are shown in **Figure 3**a. As the PDA layer thickness increased the longitudinal plasmon resonances gradually red-shifted in agreement with previous works.[26]

The calculations performed for different shell nanoparticles agree with the experimental results within ≈5% error, Figure 3a and (Table S2, Supporting Information). It is important to remember that in the actual samples, aggregation can lead to an asymmetric broadening of the transverse plasmon resonance to longer wavelengths (see Figure 1g) and a blueshift of the longitudinal plasmons.[55] Taking aggregation also into account, it is expected to eliminate any significant mismatch between theory and experiment.

Next, we proceed with the calculation of plasmonic enhancement (Figure 3b, up). The EM field norm relative to the amplitude of the incident field takes a maximum value of ≈2 for 30 nm PDA thickness, 520 nm laser wavelength, and transverse polarization (incident electric field vertical to NR long axis). The EM field becomes maximum at the Au/PDA interface and can promote charge transfer or direct interfacial optical transitions. However, the plasmonic enhancement is limited despite using resonant light. For the same light wavelength and polarization, the EM losses (Figure 3b, down) are in the order of 10^{10} W m^{-3} for 20 mW power, and 1 cm focus diameter. The EM losses are mostly localized in Au, but PDA also significantly contributes to absorption, especially at short wavelengths (Figure 3c, up) and off-resonant wavelengths (Figure 3c, down). The simulations were repeated

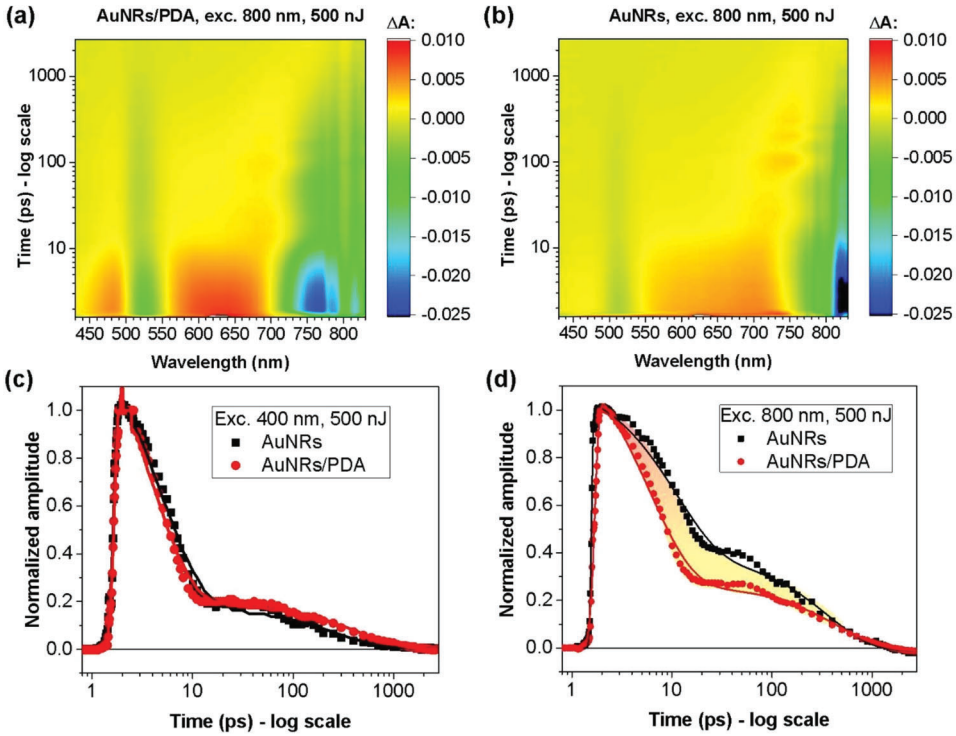

Figure 4. TA color plots for AuNRs/PDA a) and AuNRs b) Samples under 800 nm, 500 nJ excitation. Comparison of 1st SV kinetics from TA global analysis and 2-exponential fits for the samples with and without PDA for 400 nm c) and 800 nm d) excitation. Time zero is arbitrary shifted to ≈1.5 ps to better show the data in the logarithmic scale.

for all wavelengths in the 300–1100 nm range and for both transverse and longitudinal polarization (incident electric field parallel to NR long axis). The power distributed to each wavelength is calculated according to the spectrum and intensity of the lamp used for the photodegradation experiments. The total EM losses found with this procedure are shown in Figure 3d. As the PDA layer becomes thicker, the total absorption is rising due to the considerable absorption of PDA close to the maximum of the lamp spectrum (≈550 nm, see Figure S3, Supporting Information).

To estimate the temperature rise, the EM losses were used as heat sources for heat transfer calculations.[56] In this study, light intensities are too low to induce significant localized, ultrafast heating close to the nanorods (Figure S4, Supporting Information). However, the entire ensemble of NRs will induce a discernible global heating of the aqueous solution in the ≈1 h timescale (Figure S5, Supporting Information). The gold concentration is 7 μg mL^{-1}, corresponding to ≈$40 \cdot 10^9$ NRs mL^{-1} and allows us to transform the EM losses per nanostructure, to EM losses per volume of the solution and to perform simulations of macroscopic heat flow. The simulations and the experiments (Figure 3e) show that AuNRs produce measurable macroscopic heating even in the absence of nanoscale heating.

Therefore, our calculations suggest that considering the limited localized heating and plasmonic enhancement observed, the primary role of Au NRs during photodegradation is the transfer of electrons and holes to PDA. Thus, it is important to investigate the dynamics and particularities of the charge transfer process. For this task, we employ femtosecond transient absorption spectroscopy.

3.4. Femtosecond Transient Absorption Spectroscopy

A few previous studies have shown that PDA plays an electron scavenging role,[11] and some studies have shown that due to the S-scheme heterojunction formed between PDA and semiconductors, electrons are quickly transferred and stored in the PDA layer for further chemical interactions.[57] Though no metal/PDA interface has been studied, our experiments suggest that similar behavior is present at the Au/PDA interface. More importantly, in our case, photodegradation performance improvement with PDA thickness is not related to electron tunnelling effects. Here, we performed fs-TAS measurements on AuNRs/PDA and bare AuNRs. Samples were dispersed in water and excited at different wavelengths (400 and 800 nm) and two different pump pulse energies (50 and 500 nJ).

As expected for gold particles, the transient absorption spectra in the analyzed 430–830 nm range are dominated by the photoinduced broadening of the plasmonic resonance bands at 525 nm (VIS) and 780–900 nm (IR). Such broadening manifests in TA as characteristic bleach (negative amplitudes) at the centers of the bands and positive amplitudes on the wings (**Figure 4**a,b; Figure S11, Supporting Information). Therefore, the decay of the signals reflects the dominant thermalization processes of photogenerated hot electrons.[24,58,59] It can also be mentioned that the positive signal below 500 nm can be partially attributed to the interband transition modulation effect.[60]

Results show that upon excitation at 800 nm, the bare Au nanorods show a small contribution of VIS bleach-

Table 3. Time constants from TA global analysis (fast τ_1 and slow τ_2 components, the relative errors are ≈10%, based on repeated measurements for the same systems)..

Sample:	Au NRs		Au NRs/PDA	
Excitation conditions:	τ_1 (ps)	τ_2 (ps)	τ_1 (ps)	τ_2 (ps)
400 nm, 500 nJ	4.6	250	3.7	470
400 nm, 50 nJ	1.8	190	1.7	430
800 nm, 500 nJ	11	370	5.5	440
800 nm, 50 nJ	2.6	180	2.1	380

ing, while Au nanorods with PDA exhibit a much higher ratio of VIS/NIR bleach amplitudes (Figure S12, Supporting Information). This might suggest that the coupling between both plasmon resonances in nanorods (longitudinal and transversal oscillations) is higher upon PDA addition, which might be beneficial for photocatalytic response at NIR and photo-thermal effects observed in the particles.

To analyze the dynamics in AuNR, 2-exponential function was fitted to the 1st SV kinetics, representing the globally most relevant contribution to the TA evolution. The dominant fast (τ_1) and the minor slow (τ_2) components correspond to the thermalization due to electron–phonon and phonon–phonon interactions, respectively.[59,61] Figure 4c,d shows examples of the kinetics and fits, while **Table 3** collects the fitted time constants. As can be seen, both time constants are always shorter for lower pump pulse energy (50 nJ vs 500 nJ), which is understandable as fewer hot electrons are generated, resulting in faster thermalization with phonons. For the same sample and pump fluence, τ_1 is shorter for the excitation at 400 than 800 nm, because there are fewer photons and lower Au absorption for 400 nm (thus, fewer electrons are generated). The time constant τ_2 is longer in the samples with PDA. This is typically associated with heat conduction/dissipation to the external matrix (here, water). It also shows that the semiconducting part captures some charges or excitons that slowly diffuse back to gold, releasing heat and giving rise to the slower τ_2. This shows that PDA coating slows down the phonon–phonon interactions in AuNR and slows down the heat diffusion into water.

Interesting conclusions can also be derived based on the variation in the dominant τ_1 component between the samples with and without PDA. For all experimental conditions (different excitation wavelengths and fluence) this component is faster for AuNRs/PDA than for bare AuNRs under the same excitation (Table 3, Figure 4c,d**)**. The probable explanation is that in the samples with PDA the ultrafast thermalization is competing with another ultrafast electron transfer channel transfer to PDA and therefore we observe an effective acceleration of the hot electron decay. Similar conclusions related to the acceleration of hot electron decay have been presented before for other interfacial systems coupled to Au.[62–64] The results support our hypothesis and suggest that electrons generated in Au, are quickly transferred to PDA, where they are available for reactions leading to the photodegradation observed in our experiment.

3.5. ROS Determination and Degradation Kinetics

In view of our photocatalytic and TAS experiments, it is clear that the degradation of Rh6G is driven by ROS.[39] Therefore, we examine different ROS by scavengers in order to elucidate the role and the amount generated.[65] As established in the literature, the following scavengers were used for given superoxide: Ethylenediaminetetraacetic acid (EDTA) for holes (h^+), isopropyl alcohol (IPA) for OH, and p-benzoquinone (BQ) for O_2^-.[65,66] We added a 10 mM concentration to the catalyst mixture in all cases.

In **Figure 5**a, we show visible light and NIR degradation results. Notice that the degradation percentage is shown without normalization, meaning that the percentages are related to the total concentration of Rh6G. On the one hand, we report that the lamp degradation shown by AuNRs/PDA3 is similar for both IPA and EDTA (≈20%). However, when BQ is used, the degradation increases up to 39%. On the other hand, the laser degradation of the nanocomposites reaches 20% for IPA, 10% for EDTA, and 25% in the case of BQ. In order to analyze the results shown in Figure 5a, it is necessary to consider the amount of Rh6G depleted without the scavengers or the relative quenching for each experiment (Δ). The degradation efficiency for our catalyst is 51% for the lamp and 25% for the laser. In the case of EDTA, the degradation for both lamp and laser are 40% showing that a similar number of holes (h^+) are generated. Furthermore, in the case of IPA, the degradation is 40% for the lamp and 80% for a laser. This suggests that the production of OH by the nanocomposites is higher in the lamp. Finally, in the last experiment with BQ as a scavenger, degradation reached 76% for the lamp and 100% for the laser. This clearly shows that O_2^- is not produced by laser and marginally by the lamp.

Nanocomposites outperform the Au bare particles and, interestingly enough, provide a higher photodegradation when excited by visible light than with laser. It is clear that both radiations produce a similar number of h^+; this means that the photodegradation in visible light is mainly driven by superior production of OH and O_2^-. The literature indicates that gold nanoparticles produce hot holes (h^+) at 2.6–2.8 eV[67] and hot electrons at 1.30 to 1.65 eV,[33] which correspond to the transversal and longitudinal and plasmon frequencies, respectively. However, it has also been experimentally shown that a small number of h^+ are produced below the threshold of the intraband transition (600 nm), and above (>640 nm).[68] This correlated with the role of h^+ on visible light but posed a question on the apparition of holes in NIR. There is no experimental evidence of the generation of OH species on gold nanoparticles,[69] except under ionizing radiation.[70] Nevertheless, it has been shown that PDA generates hydroxyl radicals under UV–vis illumination,[71] which could explain the higher rate of OH in visible light. However, it does not explain the non-negligible presence of hydroxyl in NIR.

Considering the efficiency and kinetics of the reactions, the most used model, which fits the degradation of many organic compounds (Rh6G among them) under light irradiation, is the Langmuir–Hinshelwood model Equation (1) and Equation (2)[72,73]

$$r_0 = -\frac{dC}{dt} = \frac{kK_{LH}C_0}{1+K_{LH}} = k_{app}\,C_0 \quad (1)$$

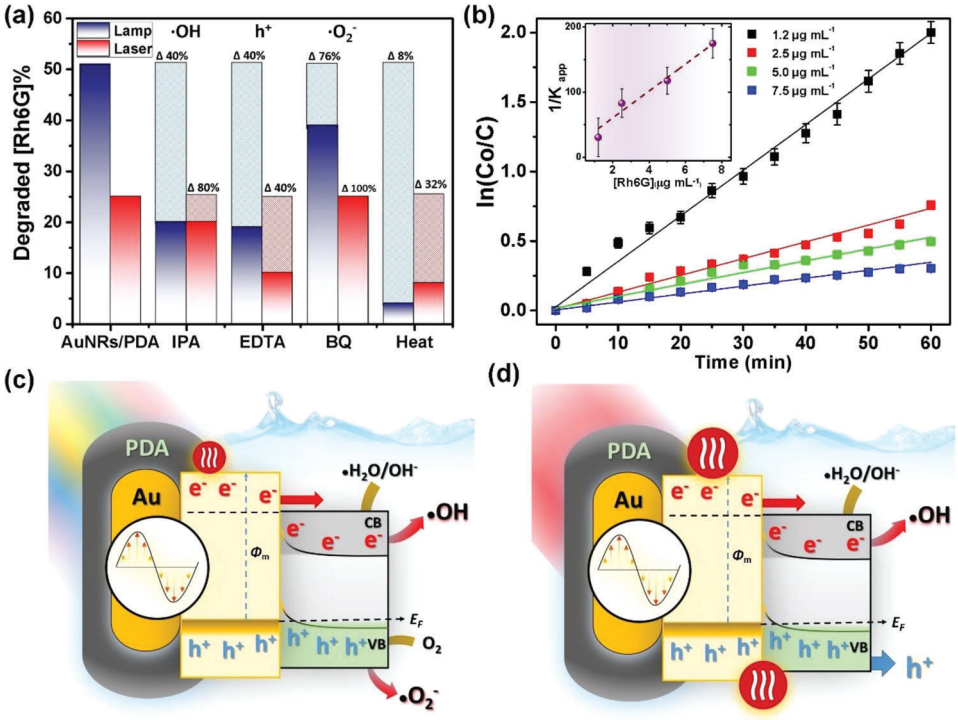

Figure 5. a) Degradation of Rh6G for lamp and laser when different scavengers are used. IPA, which quenches OH, EDTA for h^+ and BQ, which quenches O_2^-. Moreover, degradation of Rh6G is shown when no catalyst is used but only maximum temperature, reached by both lamp and laser, is applied during the catalysis. Dashed bars show the relative diminution of degradation (Δ), taking the efficiency without scavenger as 100% b) Langmuir–Hinshelwood equation and linear fit for several initial concentrations of Rh6G ($[Rh6G]_1$ = 1.2 μg mL^{-1} $[Rh6G]_2$ = 2.5 μg mL^{-1}, $[Rh6G]_3$ = 5 μg mL^{-1}, and $[Rh6G]_4$ = 7.5 μg mL^{-1}) with AuNRs/PDA3 used as nanocatalysts ($[Au]$ = 7.4 μg mL^{-1}). In–set shows the relation and linear fit between $1/K_{app}$ and [Rh6G]. c) Band model of the general production of ROS during VIS irradiation and d) during NIR irradiation. The schemes show the higher contribution of hot electrons/holes for the NIR radiation than for the visible light and depict the production products observed in the degradation experiments with scavengers.

$$\frac{1}{K_{app}} = \frac{1}{kK_{LH}} + \frac{C_0}{k} \tag{2}$$

where r_0 is the initial degradation rate of the reactant (μg mL^{-1} min^{-1}), C_0 is the initial reactant concentration (μg mL^{-1}), t is the reaction time (min) (under light irradiation), k is the reaction rate constant (μg mL^{-1} min^{-1}), K_{LH} the adsorption coefficient presented by the reactant (μg mL^{-1}), C is the reactant concentration at any time (t), and K_{app} the apparent first-order rate constant (min^{-1}). In this case, Equation (1) can be simplified for low organic dye concentrations to an apparent pseudo-first-order kinetic model shown in Equation (3).

$$\ln\left(\frac{C_0}{C}\right) = K_{app}\, t \tag{3}$$

With regards to Equation (3) and studying the kinetics of the Rh6G degradation under this Langmuir–Hinshelwood pseudo-first-order model, several photodegradation experiments with different initial concentrations of Rh6G ($[Rh6G]_1$ = 1.2 μg mL^{-1} $[Rh6G]_2$ = 2.5 μg mL^{-1}, $[Rh6G]_3$ = 5.0 μg mL^{-1}, and $[Rh6G]_4$ = 7.5 μg mL^{-1}) and the same concentration of AuNRs/PDA3 used before were carried out. Degradation plots show that the percentage of degraded [Rh6G] decays as the concentration of the organic dye is higher, being depleted 87% for $[Rh6G]_1$, 51% for $[Rh6G]_2$, 39% for $[Rh6G]_3$, and finally 26% for $[Rh6G]_4$ (Figure S13, Supporting Information). Langmuir–Hinshelwood Equation (3) is plotted in Figure 5b where the data (ln C_0/C as a function of irradiation time) can be fitted as a linear model, supporting the pseudo-first-order reaction. Calculated linear correlation equations are:

$$[Rh6G]_{1.2} \rightarrow \ln\left(\frac{C_0}{C}\right) = 33{*}10^{-3}\, t + 75{*}10^{-3} \tag{4}$$

$$[Rh6G]_{2.5} \rightarrow \ln\left(\frac{C_0}{C}\right) = 12 * 10^{-3}\, t + 24{*}10^{-3} \tag{5}$$

$$[Rh6G]_{5.0} \rightarrow \ln\left(\frac{C_0}{C}\right) = 8.5 * 10^{-3}\, t + 24{*}10^{-3} \tag{6}$$

$$[Rh6G]_{7.5} \rightarrow \ln\left(\frac{C_0}{C}\right) = 5.7 * 10^{-3}\, t + 19 * 10^{-3} \tag{7}$$

Besides, a linear plot is obtained by plotting $1/k_{app}$ versus C0, showing the consistency of the photocatalytic degradation of Rh6G offered by the Langmuir–Hinshelwood model (inset

Figure 5b). As can be observed in Equation (4) to Equation (7), k_{app} decreases as Rh6G concentration increases. This shows that the degradation occurs faster when (for the same concentration of AuNRs/PDA3) the concentration of Rh6G is lower.

Experiments performed with increased concentrations of both catalyst (22.2 μg mL^{-1}) and dye (7.5 μg mL^{-1}), for an extended experimental period (3 h) yielded a similar trend of degradation while reaching above 90% of Rh6G degradation (Figure S14, Supporting Information). To conclude this section, total organic carbon (TOC) experiments were performed on the AuNRs/PDA3 sample, and data points were collected every hour for a period of 3 h (Figure S15, Supporting Information), showing that the catalysts reached above 60% of Rh6G mineralization after 3 h, while no visible damage is observed in the nanoparticles. At similar tested concentrations, the mineralization efficiency is higher than other plasmonic nanomaterials toward Rh6G,[74] and another photocatalyst.[75]

4. Discussion

PDA coating on AuNRs is expected to improve light harvesting and decrease non-thermal radiative transitions due to the low thermal conduction of PDA, which collects light and traps heat.[76] In such a scenario, both materials should trigger the generation of reactive oxygen species,[77–79] by the absorbed heat.[20,80] Moreover, when combined, the Au plasmons pump heat into the PDA, which could, in principle, enhance and drive the production of ROS, like OH. In time, this could lead, through the carboxylation and dealkylation process, to the cleavage of multiple bonds of Rh6G hence converting Rh6G into smaller fragments and end products.[34,39] However, although heating effects are not completely overruled, as shown in Figure 5a, the results here point to a more complex mechanism in which heat is not the main driving force behind the photocatalytic degradation of contaminants.

Furthermore, considering the plasmon generation of carriers, we can assume that hot-electron-mediated photocatalysis presents some advantages, like high selectivity to specific reaction products, or reduced activation barrier.[81,82] In this type of photocatalysis, hot electrons can transfer into the conduction band of semiconductors (in this case, PDA) in two different manners. First one, via injection across the Schottky barrier (indirect plasmon-induced charge transfer) and the second one, via chemical interface damping mechanism (direct plasmon-induced charge transfer).[82] In a recent study about the degradation of organic micro-pollutants by Janus gold nanorods (Au JNRs) using visible light illumination,[34] it is suggested that plasmonic hot electrons can activate peroxide bonds and produce highly reactive free radicals, which trigger the degradation of the pollutants. According to the authors, Au JNRs absorb photons between 750 to 950 nm, which corresponds to an interval of energy between 1.30 and 1.65 eV, the strong Rayleigh scattering presented by the silica, blocks light absorption at energies that can generate hot holes (h^+) (2.6 to 2.8 eV, range between 442 and 476 nm[33]) so only hot electrons are generated.[34] Nevertheless, the enhanced reaction and reduction of contaminants observed in the Janus particles are attributed to the electron-shutting role of silica. Electrons generated in Au particles are transferred to the surface, where they can interact with dyes for further reactions, similar to the role of PDA presented here.

Our study shows that Au/PDA composites are more efficient than Au and PDA particles alone. Moreover, the efficiency of the photocatalytic effect increases with the PDA thickness Figure 2a. This clearly points to a combined phenomenon at the interface of Au/PDA. On the one hand, AuNRs present LSPR, and, as explained before, they can create hot electrons and holes within the UV–vis range.[34] Moreover, PDA possesses a high molar extinction coefficient, leading to an outstanding light absorption ability and the capability of producing ROS under visible radiation.[11,57,71,83] More importantly, our experiments have shown that the production of OH and O_2^- is higher when visible light is used and by enhancing the production of ROS, specially OH, through carboxylation and dealkylation (Figure 5c). Our TA experiments confirmed that the hot charges generated in AuNRs can be transferred to PDA on the ultrafast time scale of single ps, competing with the charge thermalization processes in gold.

On the other hand, the ROS generation in the NIR, although not as efficient as in visible light, is not negligible. Remarkably, PDA does not block the hole generation and injection, as in the case of Au/Silica but allows the transfer and injection of holes, as shown in Figure 5a, by the reduction in efficiency on the h+ scavenger. This effect is consistent with literature experiments on composites of Au and conductive polymers, where hot holes have been observed[84] and in-operando conductions with PDA and Au electrodes toward hydrogen production.[85] Therefore, the superior photothermal efficiency of Au/PDA in the NIR regime can promote ROS production (Figure 5d) in moderate, but detectable quantities.

5. Conclusion

Multimodal nanocomposites of AuNRs and PDA have been synthesized with tunable photocatalytic and photo-thermal properties. The main parameter responsible for both functionalities is the thickness of the PDA shell, which can be controlled by the concentration of the dopamine precursor during synthesis. Additionally, the PDA coating allows a controlled red shift on the Au nanorods for both longitudinal and transversal plasmons resonances.

Our studies have shown that Au/PDA nanoparticles show an excellent photocatalytic generation of ROS both in the visible and NIR regime. A macroscopic bulk water thermalization and a large generation of hot carriers accompany the processes. Furthermore, the temperature increment of the surrounding media can be controlled by the PDA thickness without hindering hot carrier transferring, which is an essential aspect of combined photo-dynamic therapies. The spectroscopic methods have shown that PDA increases the transference of hot carriers from Au to PDA, which reduces their recombination rate and shuttles the carriers toward the surface of the particles for ROS generation. We also show efficient mineralization of organic dyes and low damage of the PDA shell during photothermal and photocatalytic processes.

Finally, we have provided a mechanistic study on the applicability of Au/PDA in both photocatalysis and photo-thermal applications, with substantial implications for photodynamics therapy.

Our study shows that Au/PDA composites do provide not only local heat but also ROS production.

Supporting Information

Supporting Information is available from the Wiley Online Library or from the author.

Acknowledgements

The authors acknowledge the financial support from the National Science Centre of Poland (NCN) by the OPUS grant 2019/35/B/ST5/00248. D.A.F.: would like to acknowledge French Government Scholarship for the financial support. K.Z.: acknowledges the Program POWR.03.02.00-00-I032/16. B.G.: acknowledges the financial support from NCN by the SONATA grant number 2018/31/D/ST8/02434 in the thermal camera experiments of this article. T.V.: the numerical studies of plasmons were part of a project that had received funding from the European Union's Horizon 2020 research and innovation programme under the Marie Skłodowska-Curie grant agreement No 101003436. I.I.: acknowledges the financial support from NCN by the SONATA–BIS grant number 2020/38/E/ST5/00176 in the photodegradation experiments of this article.

Conflict of Interest

The authors declare no conflict of interest.

Data Availability Statement

The data that support the findings of this study are available from the corresponding author upon reasonable request.

Keywords

Au nanorods, nanocomposites, polydopamines, plasmons, thermal conductivity

Received: April 18, 2023
Revised: May 26, 2023
Published online:

[1] X. Huang, S. Neretina, M. A. El-Sayed, *Adv. Mater.* **2009**, *21*, 4880.
[2] K. L. Kelly, E. Coronado, L. L. Zhao, G. C. Schatz, *J. Phys. Chem. B* **2002**, *107*, 668.
[3] M. Hu, J. Chen, Z. Y. Li, L. Au, G. V. Hartland, X. Li, M. Marquez, Y. Xia, *Chem. Soc. Rev.* **2006**, *35*, 1084.
[4] M. L. Brongersma, N. J. Halas, P. Nordlander, *Nat. Nanotechnol.* **2015**, *10*, 25.
[5] M. Kim, M. Lin, J. Son, H. Xu, J. M. Nam, *Adv. Opt. Mater.* **2017**, *5*, 1700004.
[6] J. Baniukevic, I. Hakki Boyaci, A. Goktug Bozkurt, U. Tamer, A. Ramanavicius, A. Ramanaviciene, *Biosens. Bioelectron.* **2013**, *43*, 281.
[7] D. Huang, X. Bai, L. Zheng, *J. Phys. Chem. C* **2011**, *115*, 14641.
[8] J. Tian, S. Y. Deng, D. L. Li, D. Shan, W. He, X. J. Zhang, Y. Shi, *Biosens. Bioelectron.* **2013**, *49*, 466.
[9] L. X. Chen, J. J. Lv, A. J. Wang, H. Huang, J. J. Feng, *Sens. Actuators, B* **2016**, *222*, 937.
[10] Ş. Saʇlam, A. Üzer, Y. Tekdemir, E. Erçaʇ, R. Apak, *Talanta* **2015**, *139*, 181.
[11] C. G. Bailey, M. D. Nothling, L. L. Fillbrook, Y. Vo, J. E. Beves, D. R. McCamey, M. H. Stenzel, *Angew. Chem., Int. Ed.* **2023**, *62*, e202301678.
[12] J. Yu, S. Lu, W. Xu, G. He, D. He, *Appl. Organomet. Chem.* **2017**, *31*, e3785.
[13] S. Mei, Z. Kochovski, R. Roa, S. Gu, X. Xu, H. Yu, J. Dzubiella, M. Ballauff, Y. Lu, *Nano-Micro Lett.* **2019**, *11*, 83.
[14] D. D. Usta, N. Celebi, F. Soysal, A. S. Y. Saglam, N. Yildiz, K. Salimi, *Colloids Surf., A* **2021**, *611*, 125758.
[15] K. C. L. Black, J. Yi, J. G. Rivera, D. C. Zelasko-Leon, P. B. Messersmith, *Nanomedicine* **2013**, *8*, 17.
[16] S. Wang, X. Zhao, S. Wang, J. Qian, S. He, *ACS Appl. Mater. Interfaces* **2016**, *8*, 24368.
[17] B. N. Khlebtsov, A. M. Burov, T. E. Pylaev, N. G. Khlebtsov, *Beilstein J. Nanotechnol.* **2019**, *10*, 794.
[18] B. F. Grześkowiak, D. Maziukiewicz, A. Kozłowska, A. Kertmen, E. Coy, R. Mrówczyński, *Int. J. Mol. Sci.* **2021**, *22*, 738.
[19] Z. Qi, J. Shi, B. Zhu, J. Li, S. Cao, *J. Mater. Sci.* **2020**, *55*, 14530.
[20] D. Aguilar-Ferrer, J. Szewczyk, E. Coy, *Catal. Today* **2022**, *397*, 316.
[21] Y. Kim, E. Coy, H. H. J. H. Kim, R. Mrówczyński, P. Torruella, D. W. Jeong, K. S. Choi, J. H. Jang, M. Y. Song, D. J. Jang, F. Peiro, S. Jurga, H. H. J. H. Kim, *Appl. Catal. B* **2021**, *280*, 119423.
[22] W. X. Mao, X. J. Lin, W. Zhang, Z. X. Chi, R. W. Lyu, A. M. Cao, L. J. Wan, *Chem. Commun.* **2016**, *52*, 7122.
[23] S. R. Zhang, R. Bin Jiang, Y. Z. Guo, B. C. Yang, X. L. Chen, J. F. Wang, Y. F. Zhao, *Small* **2016**, *12*, 4264.
[24] M. Lorenc, M. Ziolek, R. Naskrecki, J. Karolczak, J. Kubicki, A. Maciejewski, *Appl. Phys. B* **2002**, *74*, 19.
[25] N. N. Mahmoud, H. Aqabani, S. Hikmat, R. Abu-Dahab, Á. Morcillo Alonso, J. Rubio-Retama, *mdpi.com* **2021**.
[26] B. N. Khlebtsov, A. M. Burov, N. G. Khlebtsov, *Appl. Mater. Today* **2019**, *15*, 67.
[27] E. Cortés, *Science* **2018**, *362*, 28.
[28] U. Aslam, S. Chavez, S. Linic, *Nat. Nanotechnol.* **2017**, *12*, 1000.
[29] Z. Zhang, C. Zhang, H. Zheng, H. Xu, *Acc. Chem. Res.* **2019**, *52*, 2506.
[30] H. Robatjazi, S. M. Bahauddin, C. Doiron, I. Thomann, *Nano Lett.* **2015**, *15*, 6155.
[31] M. Herran, A. Sousa-Castillo, C. Fan, S. Lee, W. Xie, M. Döblinger, B. Auguié, E. Cortés, *Adv. Funct. Mater.* **2022**, 32.
[32] S. Mukherjee, F. Libisch, N. Large, O. Neumann, L. V. Brown, J. Cheng, J. B. Lassiter, E. A. Carter, P. Nordlander, N. J. Halas, *Nano Lett.* **2013**, *13*, 240.
[33] R. Sundararaman, P. Narang, A. S. Jermyn, W. A. Goddard, H. A. Atwater, *Nat. Commun.* **2014**, *5*, 5788.
[34] H. Wei, S. K. Loeb, N. J. Halas, J. H. Kim, *Proc. Natl. Acad. Sci. USA* **2020**, *117*, 15473.
[35] X. Zhou, B. Jin, J. Luo, X. Gu, S. Zhang, *J. Solid State Chem.* **2017**, *254*, 55.
[36] A. U. Khan, Q. Yuan, Y. Wei, G. M. Khan, Z. U. H. Khan, S. Khan, F. Ali, K. Tahir, A. Ahmad, F. U. Khan, *J. Photochem. Photobiol., B* **2016**, *162*, 273.
[37] H. Zhu, X. Chen, Z. Zheng, X. Ke, E. Jaatinen, J. Zhao, C. Guo, T. Xie, D. Wang, *Chem. Commun.* **2009**, 7524.
[38] J. Gargiulo, E. Cortes, F. D. Stefani, M. Barella, I. L. Violi, L. P. Martinez, F. Goschin, V. Guglielmotti, D. Pallarola, S. Schlucker, M. Pilo-Pais, G. P. Acuna, S. A. Maier, *ACS Nano* **2021**, *15*, 2458.
[39] T. Rasheed, M. Bilal, H. M. N. Iqbal, H. Hu, X. Zhang, *Water, Air, Soil, Pollut.* **2017**, *228*, 291.
[40] Z. Zhu, M. Su, *Nanomaterials* **2017**, *7*, 160.

[41] Y. Bai, B. Zhang, L. Chen, Z. Lin, X. Zhang, D. Ge, W. Shi, Y. Sun, *Nanoscale Res. Lett.* **2018**, *13*, 1.
[42] G. Liu, Q. Xiong, Y. Xu, Q. Fang, K. C. F. Leung, M. Sang, S. Xuan, L. Hao, *Colloids Surf., A* **2022**, *633*, 127860.
[43] Y. Zhao, D. Wang, Y. Luan, X. Du, *Mater. Today Sustain.* **2022**, *18*, 100129.
[44] M. Battaglini, A. Marino, A. Carmignani, C. Tapeinos, V. Cauda, A. Ancona, N. Garino, V. Vighetto, G. La Rosa, E. Sinibaldi, G. Ciofani, *ACS Appl. Mater. Interfaces* **2020**, *12*, 35798.
[45] R. Ge, M. Lin, X. Li, S. Liu, W. Wang, S. Li, X. Zhang, Y. Liu, L. Liu, F. Shi, H. Sun, H. Zhang, B. Yang, *ACS Appl. Mater. Interfaces* **2017**, *9*, 19706.
[46] S. Liu, L. Wang, M. Lin, D. Wang, Z. Song, S. Li, R. Ge, X. Zhang, Y. Liu, Z. Li, H. Sun, B. Yang, H. Zhang, *ACS Appl. Mater. Interfaces* **2017**, *9*, 44293.
[47] Y. Jiang, M. Sun, N. Ouyang, Y. Tang, P. Miao, *ACS Appl. Mater. Interfaces* **2021**, *13*, 21653.
[48] R. Ge, X. Li, M. Lin, D. Wang, S. Li, S. Liu, Q. Tang, Y. Liu, J. Jiang, L. Liu, H. Sun, H. Zhang, B. Yang, *ACS Appl. Mater. Interfaces* **2016**, *8*, 22942.
[49] Q. Fang, K. Xu, Q. Xiong, Y. Xu, A. Hui, S. Xuan, *CrystEngComm* **2021**, *23*, 6610.
[50] J. Li, W. Wang, L. Zhao, L. Rong, S. Lan, H. Sun, H. Zhang, B. Yang, *ACS Appl. Mater. Interfaces* **2015**, *7*, 11613.
[51] M. Vega, E. M. Martín del Valle, M. Pérez, C. Pecharromán, G. Marcelo, *ChemPhysChem* **2018**, *19*, 3418.
[52] G. Loget, J. B. Wood, K. Cho, A. R. Halpern, R. M. Corn, *Anal. Chem.* **2013**, *85*, 9991.
[53] A. Kawamura, M. Kohri, G. Morimoto, Y. Nannichi, T. Taniguchi, K. Kishikawa, *Sci. Rep.* **2016**, *6*, 33984.
[54] M. Xiao, Y. Li, M. C. Allen, D. D. Deheyn, X. Yue, J. Zhao, N. C. Gianneschi, M. D. Shawkey, A. Dhinojwala, *ACS Nano* **2015**, *9*, 5454.
[55] T. Vasileiadis, A. Noual, Y. Wang, B. Graczykowski, B. Djafari-Rouhani, S. Yang, G. Fytas, *ACS Nano* **2022**, *16*, 20419.
[56] S. Manrique-Bedoya, M. Abdul-Moqueet, P. Lopez, T. Gray, M. Disiena, A. Locker, S. Kwee, L. Tang, R. L. Hood, Y. Feng, N. Large, K. M. Mayer, *J. Phys. Chem. C* **2020**, *124*, 17172.
[57] L. Wang, J. Zhang, H. Yu, I. H. Patir, Y. Li, S. Wageh, A. A. Al-Ghamdi, J. Yu, *J. Phys. Chem. Lett.* **2022**, *13*, 4695.
[58] L. Wang, D. Zare, T. H. Chow, J. Wang, M. Magnozzi, M. Chergui, *J. Phys. Chem. C* **2022**, *126*, 3591.
[59] M. Ferrera, G. D. Valle, M. Sygletou, M. Magnozzi, D. Catone, P. O'Keeffe, A. Paladini, F. Toschi, L. Mattera, M. Canepa, F. Bisio, *ACS Photonics* **2020**, *7*, 959.
[60] X. Zhang, C. Huang, M. Wang, P. Huang, X. He, Z. Wei, *Sci. Rep.* **2018**, *8*, 10499.
[61] M. Ahlawat, D. Mittal, V. G. Rao, *Commun. Mater.* **2021**, *2*, 114.
[62] H. Li, S. Wang, M. Wang, Y. Gao, J. Tang, S. Zhao, H. Chi, P. Zhang, J. Qu, F. Fan, C. Li, *Angew. Chem., Int. Ed.* **2022**, *61*, e202204272.
[63] G. Tagliabue, J. S. DuChene, M. Abdellah, A. Habib, D. J. Gosztola, Y. Hattori, W. H. Cheng, K. Zheng, S. E. Canton, R. Sundararaman, J. Sá, H. A. Atwater, *Nat. Mater.* **2020**, *19*, 1312.
[64] T. Pincelli, T. Vasileiadis, S. Dong, S. Beaulieu, M. Dendzik, D. Zahn, S. Lee, H. Seiler, Y. Qi, R. P. Xian, J. Maklar, E. Coy, N. S. Mueller, Y. Okamura, S. Reich, M. Wolf, L. Rettig, R. Ernstorfer, *Adv. Mater.* **2023**, *35*, 2209100.
[65] F. Shahsavandi, A. Amirjani, H. Reza Madaah Hosseini, *Appl. Surf. Sci.* **2022**, *585*, 152728.
[66] M. Pelaez, P. Falaras, V. Likodimos, K. O'Shea, A. A. de la Cruz, P. S. M. Dunlop, J. A. Byrne, D. D. Dionysiou, *J. Mol. Catal. A: Chem.* **2016**, *425*, 183.
[67] T. Barman, A. A. Hussain, B. Sharma, A. R. Pal, *Stem Cells Int.* **2015**, *5*, 1.
[68] S. Swaminathan, J. K. Bera, M. Chandra, *Angew. Chem., Int. Ed.* **2023**, *62*, e202215933.
[69] W. Zhang, Y. Li, J. Niu, Y. Chen, *Langmuir* **2013**, *29*, 4647.
[70] M. Misawa, J. Takahashi, *Nanomed.: Nanotechnol. Biol. Med.* **2011**, *7*, 604.
[71] Z. Wang, F. Tang, H. Fan, L. Wang, Z. Jin, *Langmuir* **2017**, *33*, 5938.
[72] H. Sudrajat, S. Babel, *Environ. Sci. Pollut. Res.* **2016**, *23*, 10177.
[73] C. P. Y. Kong, N. A. A. Suhaimi, N. N. M. Shahri, J. W. Lim, M. Nur, J. Hobley, A. Usman, *Catalysts* **2022**, *12*, 975.
[74] S. Majumder, S. Chatterjee, P. Basnet, J. Mukherjee, *J. Mol. Liq.* **2022**, *358*, 119138.
[75] S. Bae, S. Kim, S. Lee, W. Choi, *Catal. Today* **2014**, *224*, 21.
[76] K. Kang, H. Jang, Y. K. Kim, *Analyst* **2017**, *142*, 2372.
[77] M. Aioub, S. R. Panikkanvalappil, M. A. El-Sayed, *ACS Nano* **2017**, *11*, 579.
[78] V. Guerrero-Florez, S. C. Mendez-Sanchez, O. A. Patrón-Soberano, V. Rodríguez-González, D. Blach, O. F. Martínez, *J. Mater. Chem. B* **2020**, *8*, 2862.
[79] I. Singh, G. Dhawan, S. Gupta, P. Kumar, *Front. Microbiol.* **2021**, *11*, 3326.
[80] M. D'Acunto, P. Cioni, E. Gabellieri, G. Presciuttini, *Nanotechnology* **2021**, *32*, 192001.
[81] L. Zhou, D. F. Swearer, C. Zhang, H. Robatjazi, H. Zhao, L. Henderson, L. Dong, P. Christopher, E. A. Carter, P. Nordlander, N. J. Halas, *Science.* **2018**, *362*, 69.
[82] D. C. Ratchford, *ACS Nano* **2019**, *13*, 13610.
[83] V. Ball, *Catal. Today* **2018**, *301*, 196.
[84] Y. Hattori, M. Abdellah, J. Meng, K. Zheng, J. Sá, *J. Phys. Chem. Lett.* **2019**, *10*, 3140.
[85] H. Coskun, A. Aljabour, P. Luna, H. Sun, N. Nishiumi, T. Yoshida, G. Koller, M. G. Ramsey, T. Greunz, D. Stifter, M. Strobel, S. Hild, A. W. Hassel, N. S. Sariciftci, E. H. Sargent, P. Stadler, *Adv. Mater.* **2020**, *32*, 1902177.